

Role of metallic leads and electronic degeneracies in thermoelectric power generation in quantum dots

Harzheim, Achim; Sowa, Jakub K.; Swett, Jacob L.; Briggs, G. Andrew D.; Mol, Jan A.; Gehring, Pascal

DOI

[10.1103/PhysRevResearch.2.013140](https://doi.org/10.1103/PhysRevResearch.2.013140)

Publication date

2020

Document Version

Final published version

Published in

Physical Review Research

Citation (APA)

Harzheim, A., Sowa, J. K., Swett, J. L., Briggs, G. A. D., Mol, J. A., & Gehring, P. (2020). Role of metallic leads and electronic degeneracies in thermoelectric power generation in quantum dots. *Physical Review Research*, 2(1), Article 013140. <https://doi.org/10.1103/PhysRevResearch.2.013140>

Important note

To cite this publication, please use the final published version (if applicable).
Please check the document version above.


Copyright

Other than for strictly personal use, it is not permitted to download, forward or distribute the text or part of it, without the consent of the author(s) and/or copyright holder(s), unless the work is under an open content license such as Creative Commons.

Takedown policy

Please contact us and provide details if you believe this document breaches copyrights.
We will remove access to the work immediately and investigate your claim.

Role of metallic leads and electronic degeneracies in thermoelectric power generation in quantum dots

Achim Harzheim ¹, Jakub K. Sowa,¹ Jacob L. Swett,¹ G. Andrew D. Briggs,¹ Jan A. Mol,^{1,2,*} and Pascal Gehring^{1,3,†}

¹Department of Materials, University of Oxford, Oxford OX1 3PH, United Kingdom

²School of Physics and Astronomy, Queen Mary University of London, London E1 4NS, United Kingdom

³Kavli Institute of Nanoscience, Delft University of Technology, Delft 2628, Netherlands



(Received 12 June 2019; revised manuscript received 22 December 2019; accepted 24 December 2019; published 10 February 2020)

The power factor of a thermoelectric device is a measure of the heat-to-energy conversion efficiency in nanoscopic devices. Yet, even as interest in low-dimensional thermoelectric materials has increased, experimental research on what influences the power factor in these systems is scarce. Here, we present a detailed thermoelectric study of graphene quantum dot devices. We show that spin degeneracy of the quantum dot states has a significant impact on the zero-bias conductance of the device and leads to an increase of the power factor. Conversely, we demonstrate that nonideal heat exchange within the leads can suppress the power factor near the charge degeneracy point and nontrivially influences its temperature dependence.

DOI: [10.1103/PhysRevResearch.2.013140](https://doi.org/10.1103/PhysRevResearch.2.013140)

I. INTRODUCTION

Thermoelectric devices convert temperature differences between two metallic reservoirs ΔT into a thermovoltage V_{th} . The extent of this conversion is quantified by the Seebeck coefficient (thermopower) defined as $S = -\frac{\Delta V_{\text{th}}}{\Delta T}$. However, the Seebeck coefficient alone does not provide a good measure of conversion efficiency. In the linear response regime (i.e., for an operating temperature $T \gg \Delta T$) one should instead consider the power factor $\mathcal{P} = S^2 G$ (where G is the electrical conductance), which is proportional to the maximum power output density of the thermoelectric generator [1]. Since the seminal work of Dresselhaus and Hicks [2,3], predicting an increase of the thermoelectric efficiency with decreasing dimensionality, numerous experimental realizations of low-dimensional thermoelectric generators have been achieved [4–8]. Particularly promising are quantum-dot (QD) devices as they allow for precise control of heat and charge flows. Recently, the role of the Kondo effect, quantum-interference phenomena and coupling asymmetry in thermoelectric energy conversion, has been examined theoretically [9–13]. Additionally, recent experimental studies on QD thermoelectric devices demonstrated novel ways of reaching high thermoelectric efficiencies [14], approaching the Carnot efficiency limit [15]. However, the role of intrinsic device features, such as metallic leads, has not yet received much experimental attention.

In this paper, we experimentally study the thermoelectric properties and power factor of electrostatically controlled graphene quantum dots (GQDs). Our devices comprise few nanometer-sized GQDs located between two graphene leads which are connected to Au leads deposited on a Si/SiO₂ chip [Fig. 1(a)]. The GQDs are fabricated using feedback-controlled electroburning of a bowtie-shaped graphene constriction [16], which reliably produces quantum dots with high addition energies [17]. As shown in Fig. 1(a), to create a temperature gradient across the QD, we pass an electric current (inducing Joule heating) through a microheater located near the source electrode. We simultaneously measure the gate-dependent conductance G and thermovoltage V_{th} to avoid artificial offsets (which can lead to wrong estimates of the power factor [18]). To this end, we apply an ac voltage to the source through a resistor in series at a frequency of $\omega_1 = 91$ Hz. The heating current is applied at a frequency $\omega_2 = 17$ Hz while the thermovoltage drop over the quantum dot is measured at the second harmonic ($2 \times \omega_2$). The temperature difference between the gold contacts is obtained by a four-point resistance calibration [13,19].

When heating up one side of the device, the Fermi distribution of the “hot” contact gets broader compared to the “cold” contact, inducing a thermocurrent between the two leads. In an open circuit configuration, a thermovoltage V_{th} will build up to nullify the thermocurrent [see Fig. 1(b)].

II. RATE-EQUATION MODEL

Charge transport through a quantum dot weakly coupled to metallic leads can be described using a rate-equation (RE) approach. It models the overall transport as a sequence of electron hopping events, assigning a rate for hopping on (γ_l) and off ($\bar{\gamma}_l$) the QD [where $l = \text{L, R}$ and L (R) denotes the left (right) reservoir] [see Fig. 1(b)] [20]. Each lead is found at a temperature T_l determining the shape of the Fermi

*j.mol@qmul.ac.uk

†p.gehring@tudelft.nl

Published by the American Physical Society under the terms of the [Creative Commons Attribution 4.0 International license](https://creativecommons.org/licenses/by/4.0/). Further distribution of this work must maintain attribution to the author(s) and the published article's title, journal citation, and DOI.

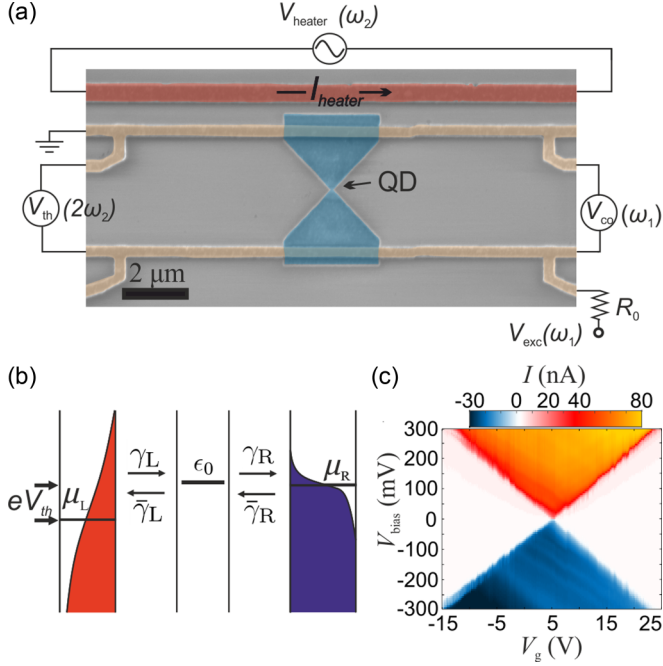


FIG. 1. (a) False-color scanning electron microscopy (SEM) image including the measurement schematics. (b) Schematic energy diagram of our device. (c) Stability diagram for device A.

distributions, $f_l = \{\exp[(\epsilon - \mu_l)/k_B T_l] + 1\}^{-1}$, where k_B is the Boltzmann constant, and μ_l the electrochemical potential of lead l . The quantum-dot energy level (located at ϵ_0) is tunnel coupled to the left and right reservoirs by Γ_l . ϵ_0 can be tuned using the gate electrode $\epsilon_0 = \epsilon_{00} - \alpha|e|V_g$, where ϵ_{00} is the position of ϵ_0 at zero gate, α is the lever arm, and V_g the gate voltage [21]. We assume that (due to strong electron-electron interactions) only one additional (transport) electron can be found on the QD at any given time. The electrical current across the QD, I , is then given by [19,22]

$$I = \frac{e}{\hbar} n_N n_{N+1} \frac{\gamma_L \bar{\gamma}_R - \gamma_R \bar{\gamma}_L}{n_{N+1}(\gamma_L + \gamma_R) + n_N(\bar{\gamma}_L + \bar{\gamma}_R)}, \quad (1)$$

where n_N and n_{N+1} are the degeneracies of the electronic ground states of N and $N + 1$ charge states, respectively. We assume that in the considered QDs only the spin degeneracy plays a role, meaning $n_N = 1$ and $n_{N+1} = 2$, or vice versa. As we will demonstrate, these factors can be extracted from the temperature-dependent shift of the conductance peak [23].

Similarly, the heat current through the dot \dot{Q} is [19]

$$\dot{Q} = \frac{n_N n_{N+1}}{\hbar} \frac{\zeta_L \bar{\zeta}_R - \bar{\zeta}_L \zeta_R}{n_{N+1}(\gamma_L + \gamma_R) + n_N(\bar{\gamma}_L + \bar{\gamma}_R)}, \quad (2)$$

where the charge and energy transfer rates in Eqs. (1) and (2) are given by

$$\bar{\gamma}_l^{(-)} = 2\Gamma_l \int \frac{d\epsilon}{2\pi} f_{\pm l}(\epsilon) K(\epsilon), \quad (3)$$

$$\zeta_l^{(-)} = 2\Gamma_l \int \frac{d\epsilon}{2\pi} f_{\pm l}(\epsilon) \epsilon K(\epsilon). \quad (4)$$

Here, lifetime broadening is introduced via the density of states of the QD, which has a Lorentzian line shape, $K(\epsilon) =$

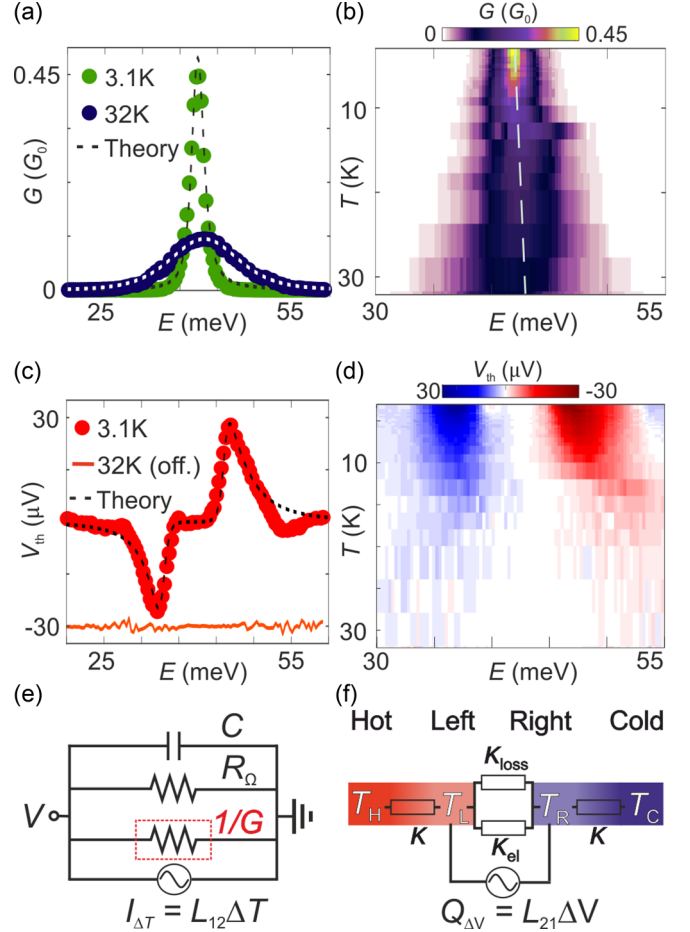


FIG. 2. (a) Conductance at 3.1 and 32 K as a function of $\alpha|e|V_g$ and the corresponding fits. (b) Conductance as a function of T and $\alpha|e|V_g$. The dashed line indicates the calculated position of the conductance peaks. (c) Thermovoltage at 3.1 and 32 K as a function of $\alpha|e|V_g$ and the corresponding fit. (d) Thermovoltage as a function of $\alpha|e|V_g$ and T . (e) Schematic of the electrical circuit driven by the thermocurrent $L_{12}\Delta T$; the red dotted line marks the device. (f) Corresponding thermal circuit diagram for our system driven by the heat current $L_{21}\Delta V$. The temperature difference for all calculations: $\Delta T = 0.52$ K.

$\Gamma/[\Gamma^2 + (\epsilon - \epsilon_0)^2]$, where $\Gamma = (\Gamma_L + \Gamma_R)/2$. The Fermi-Dirac distributions are $f_{+l}(\epsilon) \equiv f_l(\epsilon)$ and $f_{-l}(\epsilon) \equiv 1 - f_l(\epsilon)$.

III. ELECTRONIC CONDUCTANCE

Figure 1(c) shows the stability diagram of device A from which we extract the lever arm of $\alpha = 7.9$ meV. We next consider the zero-bias differential conductance $G = \frac{dI}{dV}|_{V=0}$ as a function of V_g . We begin by fitting the experimental conductance trace at $T = 3.1$ K using the rate-equation model described above [see Fig. 2(a)]. The conductance trace has an approximately Lorentzian line shape, in agreement with our model and as expected for a single-electron transistor [24]. From the fit [black dashed line in Fig. 2(a)], we obtain tunnel couplings of $\Gamma_L \approx 0.2$ meV and $\Gamma_R \approx 1.1$ meV.

Figure 2(b) shows the zero-bias conductance between 3.1 and 32 K. Two separate effects can be observed. First, the conductance peak thermally broadens and its maximum

decreases accordingly. Second, we observe that the position of the conductance peak shifts with temperature. This effect has been theoretically predicted by Beenakker [23] and can be understood as originating from changes in entropy of the system, as discussed elsewhere [25]. The semiclassical theory of Ref. [23] predicts that (for a doubly degenerate energy level as considered here) the position of the peak should shift by $\Delta E_{\text{shift}}(G_{\text{max}}) \approx \ln(2)k_B T/2$, so that $\ln(2)k_B$ can be regarded as the entropy associated with populating a doubly degenerate electronic level. This also agrees with our theory, which predicts the same shift of $\ln(2)k_B T/2$ [see the white dashed line in Fig. 2(b)].

In Fig. 2(a) we further plot the experimental (navy dots) and theoretical (white dashed line) values of the zero-bias conductance at $T = 32$ K. Both of the effects discussed above are captured well by our theoretical model (using only the parameters extracted from the 3.1 K fit). The excellent match between the experimental and theoretical values of electronic conductance also at higher temperature further supports the validity of our theoretical model.

IV. THERMOVOLTAGE

We proceed to analyze the thermovoltage measurements. As discussed, a temperature gradient across the QD is induced using the microheater shown in Fig. 1(a). V_{th} measured at 3.1 K is shown in Fig. 2(c). Similarly to the electrical conductance, the thermovoltage exhibits a gate-dependent behavior. It switches from negative to positive values as the QD energy level crosses the Fermi energy of the electrodes, indicating a change from a hole- to electron-based thermocurrent [26]. In contrast to what is predicted by the Mott relation (which connects V_{th} to dG/dV_g) [27], however, we observe a wide region of suppressed V_{th} around the charge degeneracy point. As we shall discuss, we attribute this suppression to non-ideal heat exchange within the leads resulting in a different effective temperature difference across the QD [see Fig. 2(f)]. Furthermore, as the temperature increases (from 3.1 to 32 K), the amplitude of the thermovoltage signal decreases by an order of magnitude, also in disagreement with a single-level model [13].

To explain these effects, we consider the case where the immediate contact regions coupled to the QD are at temperatures T_L and T_R , respectively, and are not perfectly thermalized with the ‘‘hot’’ and ‘‘cold’’ reservoirs at temperatures T_H and T_C , respectively [see Fig. 2(f)]. Instead, the left (right) contact is coupled to the hot (cold) reservoir via a thermal conductance $\kappa(T)$ accounting for both electrical and phononic heat transport. Additionally, the thermal conductance through the quantum dot (i.e., between left and right) consists of an electrical (gate- and temperature-dependent) contribution $\kappa_{\text{el}}(\epsilon, T)$ and a (strictly temperature-dependent) phonon/substrate contribution $\kappa_{\text{loss}}(T)$. The latter accounts for any phononic heat transport through the substrate and the QD. The resulting thermal circuit diagram is shown in Fig. 2(f). Since it is very challenging to realize perfect thermal contacts between the leads and the QD [28], we believe that similar models should be relevant to most zero-dimensional systems (although the effects may not always be as pronounced as in our study).

To quantify the interplay between heat and charge flows across the QD and determine the gate-dependent heat flow, we consider the Onsager matrix,

$$\begin{bmatrix} I \\ \dot{Q} \end{bmatrix} = \begin{bmatrix} L_{11} & L_{12} \\ L_{21} & L_{22} \end{bmatrix} \cdot \begin{bmatrix} \Delta V \\ \Delta T \end{bmatrix}, \quad (5)$$

where L_{ij} are the Onsager modes. To obtain L_{ij} , we expand I and \dot{Q} to the first order with respect to ΔT and ΔV . In the linear response regime and assuming small lifetime broadening ($\Gamma \rightarrow 0$) the modes are given by [19]

$$L_{ij} \approx -2 \frac{e^{2-i}}{\hbar k_B T} \frac{2\Gamma_L \Gamma_R}{(\Gamma_L + \Gamma_R) 3 + 3 \cosh\left(\frac{\epsilon_0}{k_B T_0}\right) - \sinh\left(\frac{\epsilon_0}{k_B T_0}\right)}, \quad (6)$$

where $n_N = 2$ and $n_{N+1} = 1$. The magnitude of the electronic heat exchange through the QD (from left to right) is given by L_{22} since the contribution of the L_{21} term can be neglected under open circuit conditions [19] so that $\kappa_{\text{el}} = L_{22}$.

First, we note that the phononic thermal transport contribution κ_{loss} dominates the thermal transport between the left and right contact off-resonance, i.e., $\kappa_{\text{el}} \ll \kappa_{\text{loss}}$ when $|\epsilon_0| \gg \Gamma, k_B T$. Far away from resonance, therefore, the effective temperature gradient across the QD ($T_L - T_R$) is determined only by κ and κ_{loss} [19],

$$T_L - T_R = r_\kappa (T_H - T_C), \quad (7)$$

where $r_\kappa = \kappa / (2\kappa_{\text{loss}} + \kappa)$.

On the other hand, accounting for all the heat-flow contributions shown in Fig. 2(f) allows us to obtain the effective temperature gradient across the QD as [19]

$$T_L - T_R = r_\kappa \frac{\kappa}{\kappa + 2L_{22} + 2L_{21}L_{12}\psi} (T_H - T_C), \quad (8)$$

where $\psi = R_\Omega / \sqrt{(R_\Omega + G)^2 + (C\omega_2 R_\Omega)^2}$. Here, $R_\Omega = 1 \text{ T}\Omega$ is the input impedance of our high-impedance amplifier, and the system capacitance is extracted from our low-temperature fit as $C \approx 3 \text{ nF}$. The zero-bias thermocurrent I_{th} is calculated using Eqs. (1) and (8). Accounting for the load resistance (R_Ω) and the inherent capacitance of the system (C) gives the thermovoltage as [19,29]

$$V_{\text{th}} = \frac{I_{\text{th}} R_\Omega}{\sqrt{(1 + R_\Omega G)^2 + (C\omega_2 R_\Omega)^2}}. \quad (9)$$

As can be inferred from Eqs. (8) and (9), the electronic heat flow across the QD, in the presence of nonideal contacts, should result in a strong suppression of the thermovoltage around resonance. This is indeed observed experimentally in Fig. 2(c) which also shows the theoretical fit of the rate-equation model (with C and ΔT as fitting parameters and $r_\kappa = 1$). The fit yields $T_L - T_R = 0.52 \text{ K}$, in good agreement with $T_H - T_C = 0.5 \pm 0.1 \text{ K}$ obtained by the contact calibration (where $T_L - T_R = T_H - T_C$ for $r_\kappa = 1$; see Sec. VI in the Supplemental Material [19]). In order to extract r_κ we fit the thermovoltage at corresponding temperatures with κ and κ_{loss} as fitting parameters and holding all other parameters constant with respect to the low-temperature fit [19]. We note that the theoretical thermovoltage is the voltage that nullifies the thermocurrent calculated from the effective temperature difference in Eq. (8).

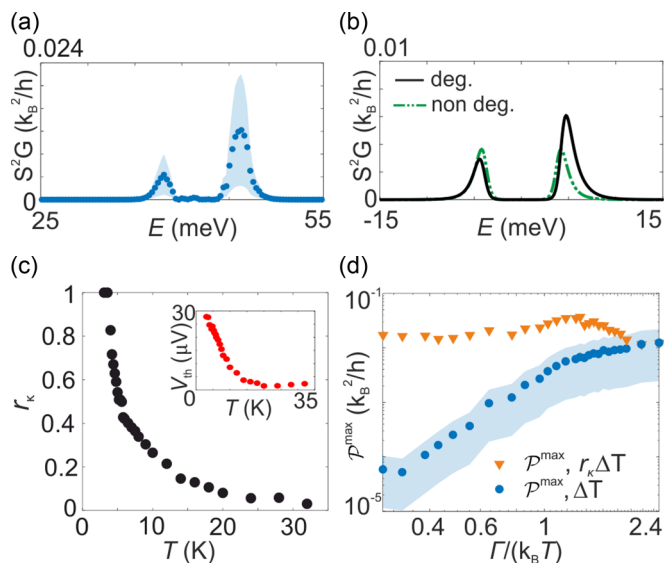


FIG. 3. (a) Experimental power factor at 3.1 K. (b) Calculated power factor for a degenerate (black line) and nondegenerate (dotted-dashed green line) energy level, holding all other parameters constant. All as a function of $\alpha|e|V_g$. (c) Ratio r_κ as a function of T . The ratio at each temperature was extracted from fits to the respective thermovoltage [19]. Inset: Maximum thermovoltage as a function of temperature. (d) Maximum power factor \mathcal{P}^{\max} as a function of T . The blue dots show \mathcal{P}^{\max} calculated with the temperature drop between the contacts (ΔT) and the orange triangles $\mathcal{P}^{\max}_{\text{eff}}$ calculated with the effective temperature drop $r_\kappa \Delta T$. In all plots a temperature difference between the two contacts of $\Delta T \approx 0.52$ K is used.

We next turn to the second nontrivial effect observed: a rapid decrease of V_{th} with increasing temperature [Figs. 2(c) and 2(d) and Fig. 3(c)]. This effect cannot be explained with a simple single-level model (within either the Landauer or RE approach) and recent experimental findings of an inverse relation studied a metallic island with a continuum of energy levels which is not applicable here [30]. Nonetheless, we note that thermovoltage decreasing with increasing temperature is almost universally reported for zero-dimensional structures [31–34]. This trend can be explained by changes in the thermal conductances (κ_{loss} and κ) between the reservoirs. As shown in Fig. 3(c) and Eq. (8), r_κ obtained from our fit and therefore the effective temperature drop over the QD ($T_L - T_R$) decreases as the temperature increases. The thermovoltage must therefore follow a similar trend. The behavior of r_κ could be attributed to a combination of the temperature-dependent thermal conductance in graphene which has a nonlinear behavior [35] and size-dependent effects due to the geometry of the device [36,37]. As the temperature is increased, the thermal conductances of the Si/SiO₂ substrate and graphene nanostructure change. The heat transport through the bulk substrate (especially the 300 μm of Si) likely dominates the overall heat transport and particularly κ_{loss} . Importantly, the thermal conductance of bulk Si increases by over an order of magnitude within the studied temperature range, which should result in a corresponding decrease of r_κ [19,38]. On the other hand, thermal conductances of the graphene electrodes are different than those of bulk graphene. As extensive theoretical

research has shown, both the magnitude and temperature dependence of the thermal conductance are very strongly dependent on the exact structure of patterned graphene [39]. We believe that, in the immediate vicinity of the quantum dot, the lead structure resembles graphene nanoribbons with multiple edge defects and dangling bonds introduced by electroburning and oxygen plasma etching. It is therefore nontrivial to predict the value (or temperature dependence) of κ , however, changes in the thermal conductivity by a factor of less than 1.5 over our temperature range as well as a decreasing thermal conductivity have been predicted for graphene nanoribbons [40]. Therefore, given the experimentally observed behavior, we conclude that the overall temperature dependence of r_κ is most likely dominated by the Si/SiO₂ substrate effects (Sec. VII in the Supplemental Material [19]). Independent of the effects discussed above, the thermovoltage line shape can be also influenced by the degeneracy of the relevant charge ground states as reported recently [41]. Electronic degeneracy can cause a slight asymmetry between the positive and negative peaks of V_{th} .

V. POWER FACTOR

We finally turn to consider the power factor, which can be obtained from the electrical conductance and thermovoltage measurements: $\mathcal{P} = S^2G = G[V_{\text{th}}/(T_H - T_C)]^2$. Figure 3(a) shows the experimental power factor obtained using G and V_{th} measured at $T = 3.1$ K. First, we note that it exhibits a clear asymmetry with respect to the charge degeneracy point. This asymmetry stems from the discussed shift of the conductance peak (since V_{th} is always zero on resonance, irrespective of temperature). Second, we observe a strong reduction of the power factor around the charge degeneracy point. This can be attributed to the effects of nonideal contacts discussed above [inducing a corresponding suppression in V_{th} ; see Eq. (8)]. Figure 3(b) shows the calculated power factor for the degenerate ($n_N = 2$ and $n_{N+1} = 1$) and nondegenerate ($n_N = n_{N+1} = 1$) QD level, keeping all other parameters constant. A good qualitative agreement between experiment and theory can be observed in the case of a degenerate electronic level.

Previously, it has been predicted that (for a noninteracting single-level model) the maximum power factor \mathcal{P}^{\max} should exhibit a maximum as a function of temperature at $k_B T \approx 1.1\Gamma$ [13]. This is a result of an interplay between S and G which are expected to increase and decrease with increasing $k_B T/\Gamma$, respectively. For the doubly degenerate level considered here, the maximum of the power factor should instead be expected to occur at $k_B T \approx 1.05\Gamma$ [19]. As we show in Fig. 3(d), however, we find that this trend is not observed experimentally (blue dots) since, in our experiments, the thermovoltage decreases with increasing T [see the inset in Fig. 3(c)]. A decreasing power factor with increasing temperature was measured in all devices included in this study, even for a less pronounced suppression of the thermovoltage signal [19]. This suggests that this is a persistent effect which needs to be taken into account when designing a high-efficiency thermoelectric QD generator.

However, when replacing the applied temperature difference ($T_H - T_C$) with the effective one, so that the effective power factor is $\mathcal{P}_{\text{eff}} = G[V_{\text{th}}/(T_L - T_R)]^2$, we recover the

expected behavior of the power factor. This is shown in Fig. 3(d) (orange triangles) where $\mathcal{P}_{\text{eff}}^{\text{max}}$ reaches a maximum for $k_{\text{B}}T \approx 1.3\Gamma$, in a relatively good agreement with the theoretical predictions.

VI. CONCLUSIONS

We investigated the influence of nonideal contacts and electronic degeneracy on the thermoelectric properties of graphene quantum dots by simultaneously measuring their thermovoltage and conductance. We have shown that the spin degeneracy of the QD level leads to a (temperature-dependent) shift in the electronic conductance peak (compared to a nondegenerate or noninteracting electronic level). As discussed, this gives rise to an asymmetric enhancement of the thermoelectric power factor. Conversely, nonideal heat exchange within the leads and heat transport through the QD were found to have a deleterious impact on the observed thermovoltage. In particular, due to an efficient electronic heat transport across the quantum dot, this effect results in a strong suppression of V_{th} in the vicinity of the charge-

degeneracy point. Our experimental results are supported by a rate-equation model which successfully captures all the phenomena described above. We believe that the effects discussed here are ubiquitous to quantum-dot thermoelectric devices. This work, therefore, opens the door to engineering zero-dimensional devices with an increased thermoelectric power factor and provides a further understanding of phenomena governing heat-to-energy conversion in such systems.

ACKNOWLEDGMENTS

This work was supported by the UK EPSRC (Grants No. EP/K001507/1, No. EP/J014753/1, No. EP/H035818/1, No. EP/K030108/1, No. EP/J015067/1, and No. EP/N017188/1). P.G. acknowledges a Marie Skłodowska-Curie Individual Fellowship under Grant TherSpinMol (ID: 748642) from the European Unions Horizon 2020 research and innovation programme. J.A.M. is a UKRI Future Leaders Fellow and acknowledges a RAEng Research Fellowship. J.K.S. thanks the Clarendon Fund and acknowledges EPSRC for the Doctoral Prize award. A.H. is supported by the Briggs Studentship.

-
- [1] W. Liu, H. S. Kim, Q. Jie, and Z. Ren, *Scr. Mater.* **111**, 3 (2016).
- [2] L. D. Hicks and M. S. Dresselhaus, *Phys. Rev. B* **47**, 16631 (1993).
- [3] L. D. Hicks and M. S. Dresselhaus, *Phys. Rev. B* **47**, 12727 (1993).
- [4] T. C. Harman, P. J. Taylor, M. P. Walsh, and B. E. LaForge, *Science* **297**, 2229 (2002).
- [5] M. Ibanez, Z. Luo, A. Genc, L. Piveteau, S. Ortega, D. Cadavid, O. Dobrozhan, Y. Liu, M. Nachttegaal, M. Zebarjadi *et al.*, *Nat. Commun.* **7**, 10766 (2016).
- [6] M.-J. Lee, J.-H. Ahn, J. H. Sung, H. Heo, S. G. Jeon, W. Lee, J. Y. Song, K.-H. Hong, B. Choi, S.-H. Lee *et al.*, *Nat. Commun.* **7**, 12011 (2016).
- [7] R. Venkatasubramanian, E. Siivola, T. Colpitts, and B. O'Quinn, *Nature (London)* **413**, 597 (2001).
- [8] J. P. Heremans, C. M. Thrush, D. T. Morelli, and M.-C. Wu, *Phys. Rev. Lett.* **88**, 216801 (2002).
- [9] R. Sanchez and M. Buttiker, *Phys. Rev. B* **83**, 085428 (2011).
- [10] M. Wierzbicki and R. Swirkowicz, *Phys. Rev. B* **84**, 075410 (2011).
- [11] M. Krawiec and K. I. Wysokinski, *Phys. Rev. B* **73**, 075307 (2006).
- [12] D. Perez Daroca, P. Roura-Bas, and A. A. Aligia, *Phys. Rev. B* **97**, 165433 (2018).
- [13] P. Gehring, A. Harzheim, J. Spièce, Y. Sheng, G. Rogers, C. Evangelini, A. Mishra, B. J. Robinson, K. Porfyrakis, J. H. Warner *et al.*, *Nano Lett.* **17**, 7055 (2017).
- [14] H. Thierschmann, R. Sánchez, B. Sothmann, F. Arnold, C. Heyn, W. Hansen, H. Buhmann, and L. W. Molenkamp, *Nat. Nanotechnol.* **10**, 854 (2015).
- [15] M. Josefsson, A. Svilans, A. M. Burke, E. A. Hoffmann, S. Fahlvik, C. Thelander, M. Leijnse, and H. Linke, *Nat. Nanotechnol.* **13**, 920 (2018).
- [16] P. Gehring, H. Sadeghi, S. Sangtarash, C. S. Lau, J. Liu, A. Ardavan, J. H. Warner, C. J. Lambert, G. A. D. Briggs, and J. A. Mol, *Nano Lett.* **16**, 4210 (2016).
- [17] P. Gehring, J. Sowa, J. Cremers, Q. Wu, H. Sadeghi, Y. Sheng, J. H. Warner, C. J. Lambert, G. A. D. Briggs, and J. A. Mol, *ACS Nano*. **11**, 5325 (2017).
- [18] Y. M. Zuev, W. Chang, and P. Kim, *Phys. Rev. Lett.* **102**, 096807 (2009).
- [19] See Supplemental Material at <http://link.aps.org/supplemental/10.1103/PhysRevResearch.2.013140> for details on thermovoltage and conductance measurements, theoretical derivation of full RE model, temperature calibration, further measurements and devices, temperature dependence of thermal conductances, and theoretical maximum power factor.
- [20] J. K. Sowa, J. A. Mol, G. A. D. Briggs, and E. M. Gauger, *J. Chem. Phys.* **149**, 154112 (2018).
- [21] R. Hanson, L. P. Kouwenhoven, J. R. Petta, S. Tarucha, and L. M. K. Vandersypen, *Rev. Mod. Phys.* **79**, 1217 (2007).
- [22] J. K. Sowa, J. A. Mol, and E. M. Gauger, *J. Phys. Chem. C* **123**, 4103 (2019).
- [23] C. W. J. Beenakker, *Phys. Rev. B* **44**, 1646 (1991).
- [24] L. P. Kouwenhoven, N. C. van der Vaart, A. T. Johnson, W. Kool, C. J. P. M. Harmans, J. G. Williamson, A. A. M. Staring, and C. T. Foxon, *Z. Phys. B* **85**, 367 (1991).
- [25] N. Hartman, C. Olsen, S. Lüscher, M. Samani, S. Fallahi, G. C. Gardner, M. Manfra, and J. Folk, *Nat. Phys.* **14**, 1083 (2018).
- [26] A. M. Lunde and K. Flensberg, *J. Phys.: Condens. Matter* **17**, 3879 (2005).
- [27] A. S. Dzurak, C. G. Smith, M. Pepper, D. A. Ritchie, J. E. F. Frost, G. A. C. Jones, and D. G. Hasko, *Solid State Commun.* **87**, 1145 (1993).

- [28] Y. Apertet, H. Ouerdane, O. Glavatskaya, C. Goupil, and P. Lecoeur, *Europhys. Lett.* **97**, 28001 (2012).
- [29] S. F. Svensson, A. I. Persson, E. A. Hoffmann, N. Nakpathomkun, H. A. Nilsson, H. Q. Xu, L. Samuelson, and H. Linke, *New J. Phys.* **14**, 033041 (2012).
- [30] P. A. Erdman, J. T. Peltonen, B. Bhandari, B. Dutta, H. Courtois, R. Fazio, F. Taddei, and J. P. Pekola, *Phys. Rev. B* **99**, 165405 (2019).
- [31] A. A. M. Staring, L. W. Molenkamp, B. W. Alphenaar, H. van Houten, O. J. A. Buyk, M. A. A. Mabesoone, C. W. J. Beenakker, and C. T. Fox, *Europhys. Lett.* **22**, 57 (1993).
- [32] L. W. Molenkamp, A. A. M. Staring, B. W. Alphenaar, H. van Houten, and C. W. Beenakker, *Semicond. Sci. Technol.* **9**, 903 (1994).
- [33] J. P. Small, K. M. Perez, and P. Kim, *Phys. Rev. Lett.* **91**, 256801 (2003).
- [34] R. Scheibner, E. G. Novik, T. Borzenko, M. König, D. Reuter, A. D. Wieck, H. Buhmann, and L. W. Molenkamp, *Phys. Rev. B* **75**, 041301(R) (2007).
- [35] J. H. Seol, I. Jo, A. L. Moore, L. Lindsay, Z. H. Aitken, M. T. Pettes, X. Li, Z. Yao, R. Huang, D. Broido, N. Mingo, R. S. Ruoff *et al.*, *Science* **328**, 213 (2010).
- [36] X. Xu, L. F. C. Pereira, Y. Wang, J. Wu, K. Zhang, X. Zhao, S. Bae, C. T. Bui, R. Xie, J. T. L. Thong *et al.*, *Nat. Commun.* **5**, 3689 (2014).
- [37] J. Hu, X. Ruan, and Y. P. Chen, *Nano Lett.* **9**, 2730 (2009).
- [38] C. J. Glassbrenner and G. A. Slack, *Phys. Rev.* **134**, A1058 (1964).
- [39] A. A. Balandin, *Nat. Mater* **10**, 569 (2011).
- [40] A. V. Savin, Y. S. Kivshar, and B. Hu, *Phys. Rev. B* **82**, 195422 (2010).
- [41] Y. Kleeorin, H. Thierschmann, H. Buhmann, A. Georges, L. W. Molenkamp, and Y. Meir, *Nat. Commun.* **10**, 5801 (2019).